nature physics

LETTERS

PUBLISHED ONLINE: 28 NOVEMBER 2010 | DOI: 10.1038/NPHYS1841

Single vortex–antivortex pair in an exciton-polariton condensate

Georgios Roumpos[1]*, Michael D. Fraser[2,3], Andreas Löffler[4], Sven Höfling[4], Alfred Forchel[4] and Yoshihisa Yamamoto[1,2]*

In a homogeneous two-dimensional system at non-zero temperature there can be no ordering of infinite range[1,2]. However, for a Bose liquid under such conditions, a superfluid phase is predicted[3–5]. Bound vortex–antivortex pairs dominate the thermodynamics and phase coherence properties in this superfluid regime. It is believed that several systems share this behaviour when the parameter describing their ordered state has two degrees of freedom[6]. This theory has been tested for some of them[7–12], but there has been no direct experimental observation of a quasi-condensate that includes a bound vortex–antivortex pair. Here we present an experimental technique that can identify a single vortex–antivortex pair in a two-dimensional exciton-polariton condensate. The pair is generated through the inhomogeneous spot profile of the pumping laser, and is revealed in the time-integrated phase maps acquired using Michelson interferometry. Numerical modelling based on the open-dissipative Gross–Pitaevskii equation suggests that the pair evolution is distinctly different in this non-equilibrium system compared with atomic condensates[13].

Microcavity exciton polaritons[14] behave as a system of strictly two-dimensional bosons when their density is below the exciton saturation density. As a result of their half-light half-matter nature, their effective mass is extremely small, so that quantum many-body effects are important at relatively high temperatures, even up to room temperature[15]. In particular, dynamic polariton condensation is observed[16–18], and its signatures are similar to Bose–Einstein condensation, namely massive occupation of the ground state and phase coherence up to large distances. However, the short lifetime allows only the formation of a quasi-equilibrium steady state, in which polaritons escaping from the cavity are continuously replenished by the external pump through an intermediate reservoir state.

Here, we show that single vortex–antivortex pairs can be observed in an exciton-polariton condensate. We have created a pumping spot that generates a minimum of the condensate density at the centre. A zero in density can be thought of as a superposition of a vortex and antivortex that can be separated by an external perturbation[19]. Thus, the centre of the condensate acts as a source of vortex–antivortex pairs. We have found that for a particular condensate size, there is on average one pair at any time. A Michelson interferometer is used to reconstruct the time-integrated phase map of the system. When the sample disorder potential is stronger than the blueshift induced by polariton–polariton interactions, pinned pairs appear at certain locations. When the sample disorder potential is weak, on the other hand, they are mobile. They appear along a fixed axis, because of a small asymmetry in the pumping spot, and are created with a random polarization, namely the vortex can appear on the right side of the spot and the antivortex on the left, or vice versa. In the time-integrated measurement, two distinct characteristic phase defects appear in both cases.

We have applied an open-dissipative Gross–Pitaevskii equation model similar to that in ref. 20, which reproduces the observed density minimum at the condensate centre. We also found that vortex–antivortex pair motion is significantly modified because of the dissipative nature of the polariton condensate and the repulsive interactions between condensate and reservoir particles. The vortex pair is found to migrate perpendicular to its dipole moment and, in our experimental parameter space, recombines before reaching the condensate edge (see Supplementary Information). Despite the short polariton lifetime, a vortex pair survives for a long enough time to be observed.

Our experiment is carried out in a GaAs-based microcavity sample[21,22]. The pump laser at above bandgap energy creates free electon–hole pairs, which form excitons and finally relax towards the lower polariton branch, as shown in the schematic of Fig. 1a. When a lower polariton decays, it emits one photon, which we observe. We employ a commercial beam shaper to create a flat-top pumping spot (see Supplementary Fig. S5). Figure 1b shows measured luminescence below threshold, which features Airy-function-like patterns because of diffraction effects. We assume that the shape is the same as the laser pumping spot, and use it as an input to our numerical calculation. Above the condensation threshold, a population dip develops at the condensate centre, as shown in the measured luminescence image of Fig. 1d. Our numerical simulation reproduces the observed population dip (Fig. 1d), and suggests that the inhomogeneity of the pump spot profile, notably the ring near the centre, generates this condensate shape. The condensate density minimum is stabilized by the repulsive reservoir–condensate interaction, because the reservoir shows a corresponding density maximum at the same point (Fig. 1c). This density minimum can be considered as an overlapping vortex and antivortex.

Phase fluctuations[23] of the condensate are responsible for the spontaneous vortex pair generation[19], and are locally maximized at the condensate centre, where the condensate density is minimum and the non-condensate density (reservoir polaritons) is maximum (see Supplementary Section S2.4). The mean-field interaction energy due to the reservoir is maximum at the centre, where the reservoir density is maximum. As power fluctuations of our

[1]E. L. Ginzton Laboratory, Stanford University, Stanford, California, 94305, USA, [2]National Institute of Informatics, Tokyo, 101-8430, Japan, [3]Institute for Nano Quantum Information Electronics, University of Tokyo, Tokyo, 153-8505, Japan, [4]Technische Physik, University of Würzburg, Physikalisches Institut and Wilhelm-Conrad-Röntgen-Research Center for Complex Material Systems, Würzburg, 97074, Germany. *e-mail: roumpos@stanford.edu; yyamamoto@stanford.edu.

© 2011 Macmillan Publishers Limited. All rights reserved.

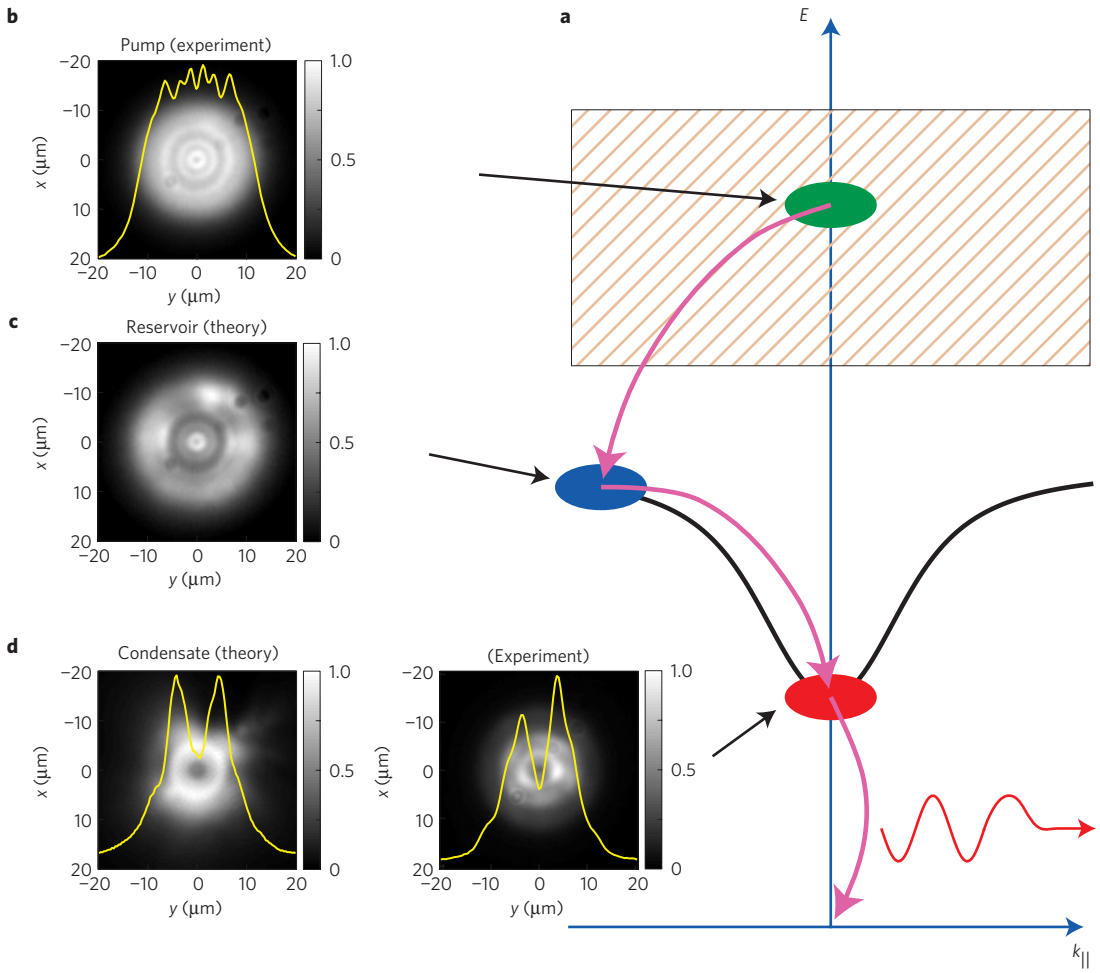

Figure 1 | Pump and condensate profile. a, Schematic of the pumping mechanism (see text). **b**, Lower-polariton luminescence image at half the threshold power. The profile along $x = 0$ is shown by the yellow line. We assume that it has the shape of the laser pumping spot, and use it as an input to our numerical simulation. **c**, Numerically calculated reservoir density above threshold. **d**, Calculated and measured condensate density images for pumping power three times above threshold.

multimode pump laser modulate the reservoir population strongly, this results in modulation of the local interaction energy and thus of the local phase of the condensate, which induces a separation of the vortex and antivortex. We confirmed that a vortex–antivortex pair is not regularly generated when a quiet single-mode pump laser is used[22]. We also note that thermal effects are not strong enough to spontaneously create a vortex–antivortex pair in our system.

We use a Michelson interferometer to reconstruct the phase map of the condensate. A schematic of the set-up is shown in Fig. 2a. We can overlap the real-space image with its reflected version on the camera, and because the two phase fronts are tilted with respect to each other, an interference pattern is observed (Fig. 2b). Changing the difference in the interferometer arm lengths shifts the fringes on the camera. Therefore, the intensity measured at one particular pixel shows a sinusoidal modulation (Fig. 2c). This reveals two pieces of information: the relative phase of the two overlapping images at this pixel point as well as the fringe visibility, which corresponds to the first-order spatial correlation function. Repeating this procedure for every pixel point, we can construct both phase and fringe visibility maps.

The expected phase map for a pinned vortex–antivortex pair is shown in Fig. 3a. If we carry out an interferometry measurement, in the way described above, with this phase map as an input, the expected result is Fig. 3b. The two double-dislocation patterns, one at the upper part, and the other at the lower part of the figure, mark the position of the pair in the original and in the reflected images. Figure 3c shows a phase map measured experimentally. It features the double-dislocation pattern characteristic of a pinned vortex–antivortex pair. In Fig. 3d, we have subtracted the global phase slope to reveal the actual phase map of a single vortex–antivortex pair, corresponding to the expected one (Fig. 3a).

In this case (Fig. 3c,d), owing to the sample disorder potential, the pair has a pinned position and polarization, defined as the vector pointing from the antivortex to the vortex. This is similar to the experiment in ref. 20, where single vortices pinned by the disorder potential were observed. However, the disorder potential in our sample is very weak generally, much smaller than the blueshift due to polariton–polariton interactions (see Supplementary Figs S10 and S6), so the disorder is screened when the condensate is formed[24]. Therefore, there are only a few locations where pinned vortex–antivortex pairs can be observed. If we mount the sample carefully, to minimize strain (see the Methods section), we can no longer find any pinned vortex pair.

We next numerically study the evolution of a mobile vortex pair imprinted along the horizontal axis, using a time-dependent open-dissipative Gross–Pitaevskii equation[25]. In a harmonically trapped conservative condensate, a single vortex pair will undergo linear motion with velocity $v_{v-av} = \hbar/md_v$, which is inversely proportional to the vortex–antivortex separation d_v, and on interaction with the boundary will wrap back on itself with a

© 2011 Macmillan Publishers Limited. All rights reserved.

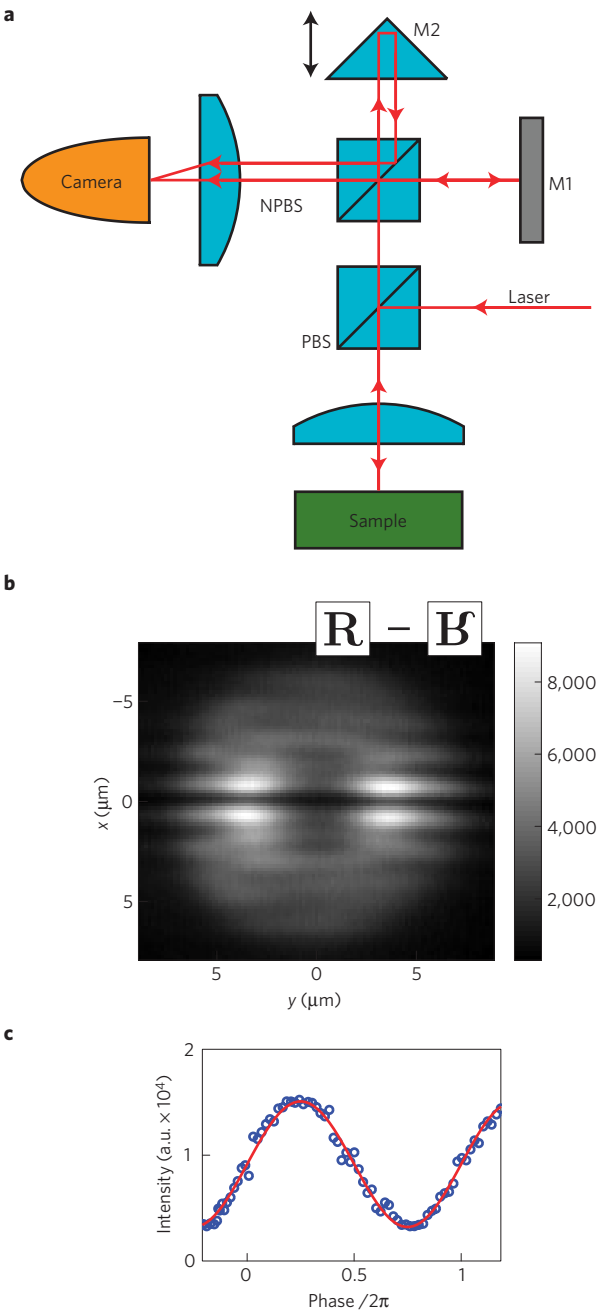

Figure 2 | Michelson interferometer. a, Schematic of the set-up for measurement of phase and fringe visibility maps. It employs a mirror (M1) and a right-angle prism (M2), which creates the reflection of the original image along one axis, depending on the prism orientation. A two-lens microscope set-up overlaps the two real-space images of the polariton condensate on the camera. PBS: polarizing cube beam splitter; NPBS: non-polarizing cube beam splitter. **b**, Typical interference pattern observed above the polariton condensation threshold (at 60 mW) along with a schematic showing the orientation of the two overlapping images. **c**, Blue circles: intensity on one pixel of the camera as a function of the prism (M2) position in normalized units. Red line: fit to a sine function.

cyclical motion. However, a polariton condensate with considerable repulsive condensate–reservoir interaction (due to the large reservoir population present in the experiment) experiences drag forces strongly perturbing the vortex pair motion[26], causing it to recombine after only a short travel distance. For these types of micro-motion, despite the vortex pair motion, a signature of the pair in the time-integrated interferogram is preserved. There are two areas where the phase is shifted by π, one at the top and the other at the bottom of the figure, and they are surrounded by minima in the fringe visibility. The measured positions of the phase defects depend on the time-averaged positions of the vortex and antivortex. The calculated time-integrated phase and visibility maps for such a moving pair are shown in Fig. 4a and b respectively.

We indeed observed such unique patterns experimentally when the sample strain was removed, as shown in Fig. 4c,d, which illustrates typical experimental data. In Fig. 4e, we have not subtracted the global phase slope, so that the direct experimental phase map is given. In Fig. 4f, we plot the cross-section of the phase along two (solid and dashed) lines passing through the two areas of π-phase shift, where this phase shift is shown quantitatively. We also plot the measured fringe visibility along the same lines, and find that the visibility minima coincide with the phase jumps. This result demonstrates that the vortex–antivortex pairs are created with a random polarization after the removal of strain. Moreover, when we rotate the prism by 90°, so that the reflected image is along the vertical axis, no phase defect is observed (Fig. 4g). The difference between Fig. 4e and g can be understood as follows: the vortex pair always remains on the horizontal axis and we fold the reflected image along the vertical axis. In this case, the phase rotation around the vortex by 2π and that around the antivortex by −2π cancel out; thus, there is no phase defect in the interference pattern (see Supplementary Fig. S13). The corresponding visibility map without any defect is shown in Fig. 4h.

The free pair of Fig. 4 shows a distinct signature compared with the pinned pair of Fig. 3. Indeed, in the interferogram of Fig. 3d there are two singularity points, one at the location of the vortex, and the other at the location of the antivortex, and the measured phase is continuous everywhere else. The experimental data in Fig. 4 suggest that such vortex–antivortex pairs are not pinned and travel a distance comparable to the spot size in a process similar to the one described in ref. 27. When the pair can form with random polarization and also move, the measured time-integrated interferogram is a superposition of many interferograms of the same type as Fig. 3d with varying positions for the vortex and antivortex. This results in a pattern with two π-phase shift areas (Fig. 4c), which is consistent with our theory (Fig. 4a).

We consistently observe pairs along the same axis, even after we rotate the sample by 90°. However, when we rotate the pump laser spot by 90°, the polarization axis of the vortex pair is also rotated by 90° as shown in Supplementary Fig. S9. These results suggest that the pair polarization direction is determined by a small asymmetry of the pump laser spot, rather than by the disorder potential landscape in the sample. Although the pair orientation follows the rotation of the laser spot, the random switching of pair polarization confirms that the pair generation mechanism is non-deterministic. We found that there is no noticeable dependence of the measured phase maps on the laser pumping power, up to ∼5 times the threshold power. Finally, we have created a Gaussian pumping spot and did not observe any phase defects (Supplementary Fig. S7). This observation supports our argument that the minimum of the condensate density at the centre of the spot acts as a source of vortex–antivortex pairs. Given that the condensate size is not much larger than the size of the vortex pair, it is not possible for more than one pair to enter into the system. Indeed, no phase defects are observed in a smaller condensate (Supplementary Fig. S8).

Our results suggest that vortex–antivortex pairs can be created in a two-dimensional condensate without rotation or stirring, although thermal fluctuations are not believed to play any role in pair generation in our system. Further measurements on larger condensates containing more vortex–antivortex pairs should clarify the influence of pair dynamics on phase coherence and polariton superfluidity[20,21,28–31].

© 2011 Macmillan Publishers Limited. All rights reserved.

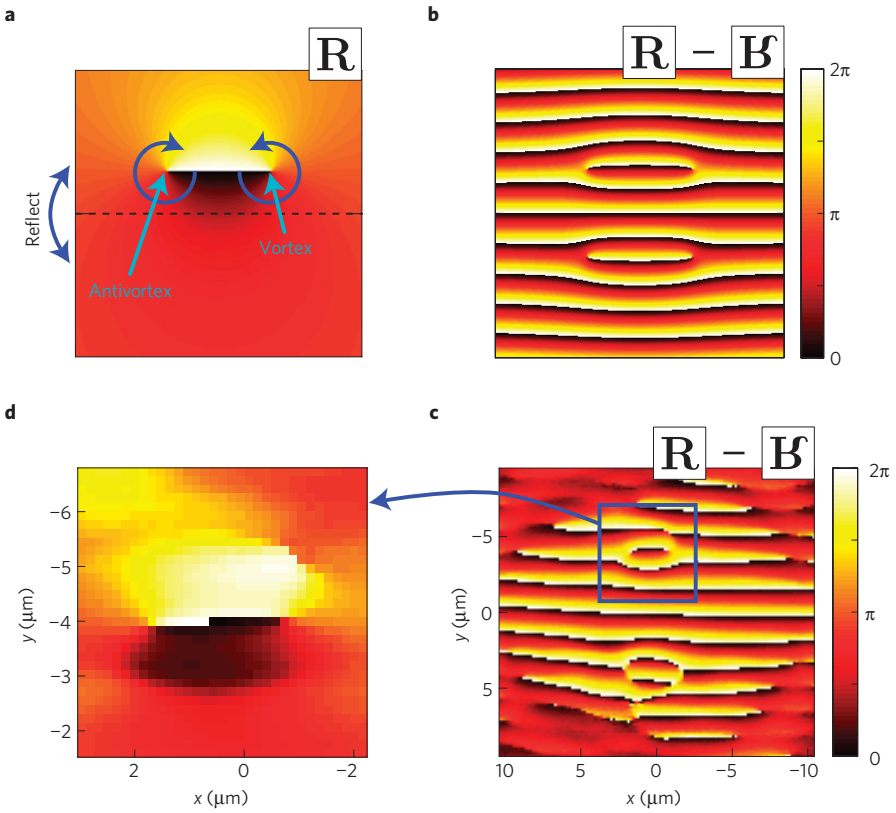

Figure 3 | Phase map of a pinned pair. a, Expected phase map of a condensate including a single vortex–antivortex pair. The arrows show the direction of the phase increase around the vortex and antivortex. **b**, Simulation of the experimentally measured phase map when **a** interferes with its reflection along the horizontal (dashed) line. A global phase slope along the vertical direction is added. **c**, Experimentally measured phase map at 55 mW above the condensation threshold of 20 mW. The blue square marks the position of a double-dislocation pattern. **d**, Expanded view of the blue square in **c**, where the global slope along the horizontal direction is subtracted. **c** and **d** are rotated by 90° with respect to all other experimental data.

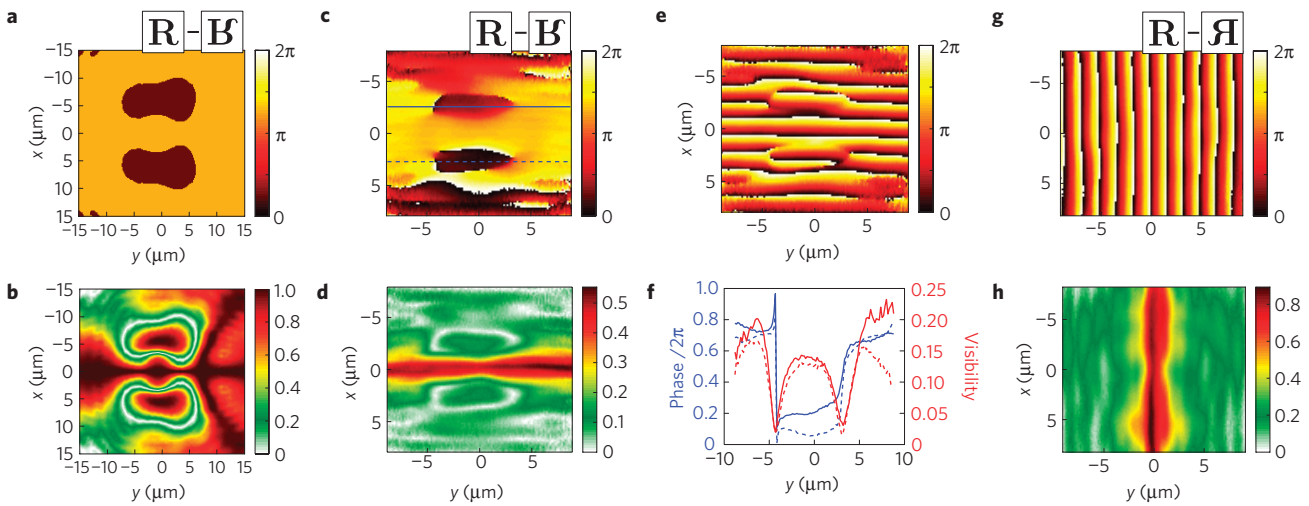

Figure 4 | Phase and fringe visibility map of a free pair. a, Theoretical time-integrated phase map for a vortex–antivortex pair imprinted onto a condensate and evolving according to the dissipative Gross–Pitaevskii equation. **b**, Corresponding fringe visibility map. **c**,**d**, Measured phase and fringe visibility maps. **e**, The same as in **c**, but now the global phase slope is not subtracted. **f**, Blue: phase cross-section along the solid and dashed lines in **c**. Red: fringe visibility cross section along the same lines. **g**, Measured phase map when the prism is rotated by 90°, along with a schematic showing the orientation of the interfering images. **h**, Corresponding fringe visibility map. Experimental data are taken at 55 mW, above the condensation threshold of 20 mW.

Methods

Michelson interferometer. We employ a commercial refractive beam shaper (Newport) to create a flat-top pumping spot. The laser pump is vertically polarized and is focused on the sample through a polarizing cube beam splitter (see Supplementary Information). Luminescence of the orthogonal linear polarization is detected and split into two parts by a 50–50 non-polarizing cube beam splitter. We use a dielectric mirror for the first arm of the interferometer, and an uncoated glass right-angle prism for the second one. The position of the prism is controlled by a combination of a translation stage and a piezoelectric actuator. Our imaging system combines a high-numerical-aperture objective lens (NA = 0.55) with a

© 2011 Macmillan Publishers Limited. All rights reserved.

plano-convex lens and offers a magnification of ×50. The image is focused on a high-resolution electron-multiplying CCD (charge-coupled device) camera with a pixel size of $8 \times 8\,\mu m^2$ (Andor). In front of the camera, we use a combination of two interference filters, one long-pass at 750 nm and one band-pass at 770 ± 5 nm, which block the laser wavelength without distorting the signal spectrum.

Sample. Our microcavity sample features a $\lambda/2$ AlAs cavity with three stacks of 4 GaAs quantum wells at the central three antinodes of the resonant electric field. It shows a Rabi splitting of $2\hbar\Omega_R = 14$ meV. Measurements are carried out for photon–exciton detuning $\delta \sim 0$ meV, which gives an effective mass for lower polaritons of $m^*_{LP} \sim 5 \times 10^{-5} m_e$. From the linewidth of the reflection dip as well as from measurement of time-resolved luminescence, we estimate the lower-polariton lifetime to be $\tau_{LP} \sim 4$ ps. The sample is mounted using silver paint on a copper sample holder, attached to the cold finger of a helium flow cryostat. The energy splitting between orthogonally polarized luminescence at 0° collection angle (ground-state splitting ΔE_{gr}) can be up to 150 μeV. However, when special care is taken to reduce strain during cooldown, by applying a homogeneous layer of silver paint between the sample and the sample holder, the ground-state splitting can be reduced below 50 μeV. Data in Fig. 3 are taken with $\Delta E_{gr} = 150$ μeV, whereas all other data, including Supplementary Information, are taken with $\Delta E_{gr} \leq 50$ μeV. In the latter case, luminescence above threshold is weakly linearly polarized along the direction of minimum energy, with a degree of linear polarization ≤20%.

Laser. We pump the sample with a mode-locked Ti:sapphire laser (Coherent) operated in the continuous-wave mode. To avoid sample heating, we use an optical chopper to modulate the laser in 0.5 ms pulses at 100 Hz repetition rate. The laser is incident from the normal direction and its wavelength is at the first reflectivity minimum of the microcavity above the stop band (723 nm). The incident power is controlled by a polarization filtering set-up employing a variable retarder, as in ref. 22. The threshold power of 20 mW (see Supplementary Information) gives a threshold particle density of $\sim 10^2\,\mu m^{-2}$ for our 20-μm-diameter pumping spot, given the 4 ps lower-polariton lifetime, and estimated pumping efficiency of 15%.

Theoretical model. The open-dissipative Gross–Pitaevskii equation[20,25] consists of two coupled equations describing the time evolution of the condensate order parameter $\psi(\mathbf{r},t)$ and reservoir polariton density $n_R(\mathbf{r},t)$

$$i\hbar\frac{\partial\psi(\mathbf{r},t)}{\partial t} = \left(-\frac{\hbar^2\nabla^2}{2m_{LP}} - \frac{i\hbar}{2}[\gamma_C - R(n_R(\mathbf{r},t))] + g_C|\psi(\mathbf{r},t)|^2 + g_R n_R(\mathbf{r},t)\right)\psi(\mathbf{r},t)$$

$$\frac{\partial n_R(\mathbf{r},t)}{\partial t} = P_l(\mathbf{r},t) - \gamma_R n_R(\mathbf{r},t) - R(n_R(\mathbf{r},t))|\psi(\mathbf{r},t)|^2$$

$n_R(\mathbf{r},t)$ is controlled by laser pumping gain $P_l(\mathbf{r})$ and reservoir loss γ_R. Interaction between condensate and reservoir is assigned a coupling constant $g_R = 2g_C$, where the condensate coupling constant is $g_C = 6 \times 10^{-3}$ meV μm^2. Other parameters are the condensate polariton loss rate $\gamma_C = 0.33\,ps^{-1}$, and stimulated scattering rate $R(n_R(\mathbf{r},t))$. The strong influence of the reservoir population on the condensate spatial profile allows us to indirectly probe the reservoir population density and uniquely determine the parameter space. In particular, we obtain best fits to experimental sequences of real-space data as a function of P_l (see Supplementary Fig. S14) for pumping threshold $P_{th} = 25$ mW with 24% pumping efficiency and $\gamma_R \approx 1.5\gamma_C$ and $R(n_R(\mathbf{r},t))/n_R(\mathbf{r},t) \approx \gamma_C\gamma_R/P_{th}$. To study the vortex pair dynamics, a vortex and antivortex are imprinted onto a steady-state condensate directly through a phase factor $e^{i\vartheta}$ along the horizontal axis, and are subsequently left free to evolve in time. The temporal frames are stored and then cumulatively subjected to the same time-averaging mechanism as in the experiment.

Received 30 April 2010; accepted 8 October 2010; published online 28 November 2010; corrected online 2 December 2010

References

1. Hohenberg, P. C. Existence of long-range order in one and two dimensions. *Phys. Rev.* **158,** 383–386 (1967).
2. Mermin, N. D. & Wagner, H. Absence of ferromagnetism or antiferromagnetism in one- or two-dimensional isotropic Heisenberg models. *Phys. Rev. Lett.* **17,** 1133–1136 (1966).
3. Berezinskii, V. L. Destruction of long-range order in one-dimensional and two-dimensional systems possessing a continuous symmetry group. II. Quantum systems. *Sov. Phys. JETP* **34,** 1144–1156 (1972).
4. Kosterlitz, J. M. & Thouless, D. J. Ordering, metastability and phase transitions in two-dimensional systems. *J. Phys. C* **6,** 1181–1203 (1973).
5. Posazhennikova, A. Weakly interacting, dilute Bose gases in 2D. *Rev. Mod. Phys.* **78,** 1111–1134 (2006).
6. Kosterlitz, J. M. & Thouless, D. J. Two-dimensional physics. *Prog. Low Temp. Phys.* **VII B,** 371–433 (1978).
7. Bishop, D. J. & Reppy, J. D. Study of the superfluid transition in two-dimensional ^{4}He films. *Phys. Rev. B* **22,** 5171–5185 (1980).
8. Resnick, D. J., Garland, J. C., Boyd, J. T., Shoemaker, S. & Newrock, R. S. Kosterlitz–Thouless transition in proximity-coupled superconducting arrays. *Phys. Rev. Lett.* **47,** 1542–1545 (1981).
9. van der Zant, H. S. J., Rijken, H. A. & Mooij, J. E. Phase transition of frustrated two-dimensional Josephson junction arrays. *J. Low Temp. Phys.* **82,** 67–92 (1991).
10. Safonov, A. I., Vasilyev, S. A., Yasnikov, I. S., Lukashevich, I. I. & Jaakkola, S. Observation of quasicondensate in two-dimensional atomic hydrogen. *Phys. Rev. Lett.* **81,** 4545–4548 (1998).
11. Hadzibabic, Z., Krüger, P., Cheneau, M., Battelier, B. & Dalibard, J. Berezinskii–Kosterlitz–Thouless crossover in a trapped atomic gas. *Nature* **441,** 1118–1121 (2006).
12. Cladé, P., Ryu, C., Ramanathan, A., Helmerson, K. & Phillips, W. D. Observation of a 2D Bose gas: From thermal to quasicondensate to superfluid. *Phys. Rev. Lett.* **102,** 170401 (2009).
13. Neely, T. W., Samson, E. C., Bradley, A. S., Davis, M. J. & Anderson, B. P. Observation of vortex dipoles in an oblate Bose–Einstein condensate. *Phys. Rev. Lett.* **104,** 160401 (2010).
14. Weisbuch, C., Nishioka, M., Ishikawa, A. & Arakawa, Y. Observation of the coupled exciton-photon mode splitting in a semiconductor quantum microcavity. *Phys. Rev. Lett.* **69,** 3314–3317 (1992).
15. Christopoulos, S. *et al.* Room-temperature polariton lasing in semiconductor microcavities. *Phys. Rev. Lett.* **98,** 126405 (2007).
16. Deng, H., Weihs, G., Santori, C., Bloch, J. & Yamamoto, Y. Condensation of semiconductor microcavity exciton polaritons. *Science* **298,** 199–202 (2002).
17. Kasprzak, J. *et al.* Bose–Einstein condensation of exciton polaritons. *Nature* **443,** 409–414 (2006).
18. Balili, R., Hartwell, V., Snoke, D., Pfeiffer, L. & West, K. Bose–Einstein condensation of microcavity polaritons in a trap. *Science* **316,** 1007–1010 (2007).
19. Giorgetti, L., Carusotto, I. & Castin, Y. Semiclassical field method for the equilibrium Bose gas and application to thermal vortices in two dimensions. *Phys. Rev. A* **76,** 013613 (2007).
20. Lagoudakis, K. G. *et al.* Quantized vortices in an exciton–polariton condensate. *Nature Phys.* **4,** 706–710 (2008).
21. Utsunomiya, S. *et al.* Observation of Bogoliubov excitations in exciton–polariton condensates. *Nature Phys.* **4,** 700–705 (2008).
22. Roumpos, G., Nitsche, W. H., Höfling, S., Forchel, A. & Yamamoto, Y. Gain-induced trapping of microcavity exciton polariton condensates. *Phys. Rev. Lett.* **104,** 126403 (2010).
23. Petrov, D. S., Holzmann, M. & Shlyapnikov, G. V. Bose–Einstein condensation in quasi-2D trapped gases. *Phys. Rev. Lett.* **84,** 2551–2555 (2000).
24. Amo, A. *et al.* Light engineering of the polariton landscape in semiconductor microcavities. *Phys. Rev. B* **82,** 081301(R) (2010).
25. Wouters, M. & Carusotto, I. Excitations in a nonequilibrium Bose–Einstein condensate of exciton polaritons. *Phys. Rev. Lett.* **99,** 140402 (2007).
26. Fraser, M. D., Roumpos, G. & Yamamoto, Y. Vortex–antivortex pair dynamics in an exciton polariton condensate. *New J. Phys.* **11,** 113048 (2009).
27. Pigeon, S., Carusotto, I & Ciuti, C. Hydrodynamic nucleation of vortices and solitons in a resonantly excited polariton superfluid. Preprint at http://arxiv.org/abs/1006.4755v1 (2010).
28. Carusotto, I. & Ciuti, C. Probing microcavity polariton superfluidity through resonant Rayleigh scattering. *Phys. Rev. Lett.* **93,** 166401 (2004).
29. Amo, A. *et al.* Superfluidity of polaritons in semiconductor microcavities. *Nature Phys.* **5,** 805–810 (2009).
30. Wouters, M. & Savona, V. Superfluidity of a nonequilibrium Bose–Einstein condensate of polaritons. *Phys. Rev. B* **81,** 054508 (2010).
31. Sanvitto, D. *et al.* Persistent currents and quantized vortices in a polariton superfluid. *Nature Phys.* **6,** 527–533 (2010).

Acknowledgements

We thank M. Kasevich and A. L. Fetter for stimulating discussions. This work was supported by Special Coordination Funds for Promoting Science and Technology, National Science Foundation ECCS-09 25549, Navy/SPAWAR Grant N66001-09-1-2024, JSPS through its Funding Program for World-Leading Innovative R and D on Science and Technology (FIRST Program), and MEXT.

Author contributions

G.R. designed and built the experimental set-up, took and analysed the data and wrote the paper. M.D.F. carried out the numerical calculations and wrote the paper. A.L., S.H. and A.F. fabricated the microcavity sample. Y.Y. conceived the experiment. All authors contributed to data interpretation.

Additional information

The authors declare no competing financial interests. Supplementary information accompanies this paper on www.nature.com/naturephysics. Reprints and permissions information is available online at http://npg.nature.com/reprintsandpermissions. Correspondence and requests for materials should be addressed to G.R. or Y.Y.

© 2011 Macmillan Publishers Limited. All rights reserved.